



# PVP-assisted hydrothermal synthesis and photocatalytic activity of single-crystalline BiFeO<sub>3</sub> nanorods

Xiaoyi Li<sup>1</sup> · Zhixian Tang<sup>1</sup> · Haidong Ma<sup>1</sup> · Fan Wu<sup>1</sup> · Ronghua Jian<sup>1</sup>

Received: 30 April 2019 / Accepted: 31 July 2019 / Published online: 8 August 2019  
© Springer-Verlag GmbH Germany, part of Springer Nature 2019

## Abstract

One-dimensional, single-crystalline bismuth ferrite (BiFeO<sub>3</sub>) nanorods were successfully prepared by polyvinylpyrrolidone-assisted hydrothermal process. The crystal structure and morphology of the as-prepared BiFeO<sub>3</sub> sample were characterized by X-ray diffraction (XRD), field emission scanning electron microscope and transmission electron microscopy. The XRD analysis reveals that single-phase BiFeO<sub>3</sub> sample was obtained. Morphology observation shows that the as-formed BiFeO<sub>3</sub> nanoparticles are the shape of nanorods. The band gap of the as-prepared BiFeO<sub>3</sub> nanorods was identified by ultraviolet–visible diffuse reflectance spectrum. Meanwhile, the photocatalytic properties of the as-prepared BiFeO<sub>3</sub> nanorods were evaluated by degrading Rhodamine B. The result revealed that the as-prepared BiFeO<sub>3</sub> nanorods exhibit photocatalytic activity under visible light irradiation ( $\lambda \geq 400$  nm).

## 1 Introduction

Over the past few years, perovskite-type bismuth ferrite (BiFeO<sub>3</sub>, denoted as BFO), as a typical multiferroic material, became more and more attractive due to its potential applications in information storage, sensors, spintronic devices [1–3]. Recently, BFO has also been demonstrated as a promising visible-light driven photocatalyst because of its suitable band gap (2.2 eV), good chemical stability and intrinsic electric polarization field [4–6]. Many studies have been carried out on its photocatalytic ability to degrade various pollutants such as Congo red, methyl orange, methylene blue and Rhodamine B (RhB) [7–9].

The activity of a photocatalyst is closely related to its optical absorption properties (band gap), the separation efficiency of photo-induced electron–hole pairs as well as the transport of electron–hole pairs. Therefore the morphology, particle size, phase purity and crystallinity of a photocatalyst would significantly influence its photocatalytic activity. Accordingly, BFO has been prepared in many forms such as thin films, microparticles, nanoparticles and nanocomposites, and these forms have been studied for their photocatalytic activities under visible light [10–14]. However,

recent studies show that the photocatalysts in the form of one-dimensional nanostructures, such as nanotubes, nanofibers and nanowires, in comparison with bulk material, have demonstrated enhanced efficiencies for photocatalytic water splitting or Congo red [15–18]. The reduced radial dimension and the high surface-to-volume ratio promote rapid diffusion of photogenerated electrons/holes to the surfaces of nanowires before recombination can occur, and thus can improve separation efficiency of charge carriers [18, 19]. Consequently, the one-dimensional BFO nanostructures, such as nanowires [20, 21], nanotubes [22, 23] and arrays [24] of BFO, have been prepared by various methods.

The synthesis of the BFO nanorods and nanotubes commonly need anodized aluminum oxide (AAO) template [23], high voltage electrospinning techniques [25], surfactant and polymer (polyvinylpyrrolidone, PVP) auxiliary hydrothermal techniques [26]. And most BFO prepared by these methods are polycrystalline structures, which seriously affect their properties and applications. Li and his coworkers reported that the single crystal nanowire is considered to be more active because the charge transport along the wire axis is much more effective than the diffusive transport in polycrystalline material [18]. Recently, one-dimensional single-crystalline BFO nanowires and nanorods have been synthesized by hydrothermal method [20, 27]. However, it is still a challenge for scientists and engineers to synthesize one-dimensional, single-crystalline BFO nanorods in large amounts due in part to the kinetics of phase formation in the

✉ Xiaoyi Li  
xyli@zjhu.edu.cn

<sup>1</sup> College of Science, Huzhou University, Huzhou 313000, Zhejiang, People's Republic of China

$\text{Bi}_2\text{O}_3\text{-Fe}_2\text{O}_3$  system [28]. In addition, there are few reports on the application of BFO nanorods in photocatalysis. Therefore, the design of one-dimensional, single-crystalline BFO nanorods with novel and well-defined morphologies is important for both fundamental research and the application of photocatalysis.

In this work, single-crystalline BFO nanorods were prepared by polyvinylpyrrolidone (PVP)-assisted hydrothermal process. The crystal structure, surface morphology and optical properties of BFO sample were investigated. Meanwhile, the photocatalytic properties of the as-obtained BFO nanorods were evaluated by degrading Rhodamine B (RhB), one common pollutant. On the basis of these experimental results, a possible photocatalytic mechanism of BFO nanorods was critically discussed.

## 2 Experimental section

### 2.1 Fabrication of $\text{BiFeO}_3$ nanorods

Bismuth nitrate ( $\text{Bi}(\text{NO}_3)_3 \cdot 5\text{H}_2\text{O}$ ), ferric chloride hexahydrate ( $\text{FeCl}_3 \cdot 6\text{H}_2\text{O}$ ) and Rhodamine B were purchased from Aladdin Chemical Reagent. Sodium hydroxide (NaOH) and Polyvinylpyrrolidone K-30 (PVP) were obtained from Huzhou Feiyang Chemical Reagent Management Department, PR China. All chemicals were of analytical grade and used without further purification.

BFO nanorods were synthesized by a hydrothermal method, similar to a recent report by Li et al. [21]. In a typical synthesis,  $\text{Bi}(\text{NO}_3)_3 \cdot 5\text{H}_2\text{O}$  and  $\text{FeCl}_3 \cdot 6\text{H}_2\text{O}$  in a stoichiometric ratio (1:1 in molar ratios) were dissolved in ethylene glycol (50 mL, 98%) and sonicated for 30 min. Then deionized (D.I.) water (200 mL) and concentrated ammonia were added under vigorous stirring until the pH value of the solution reached 10–11. The sediment was centrifuged out and washed with DI water several times until the pH value was neutral. Next, the red co-precipitate was redispersed in 40 ml of DI water. Under vigorous stirring, 0.5 g of PVP and 8 g NaOH were added into the suspension. Next, the solution was placed inside a stainless steel autoclave with a Teflon liner and heated at 160 °C for 48 h. After cooling down to room temperature, the precipitate was collected by centrifugation, washed with DI water and absolute ethanol for several times, respectively, and then dried at 60 °C for 8 h.

### 2.2 Characterization

The obtained sample was characterized by XRD on a X'Pert PANalytical x-ray powder diffractometer with  $\text{Cu K}\alpha$  radiation ( $\lambda = 1.54060 \text{ \AA}$ ) operated at 40 kV and 40 mA in the  $2\theta$  range of  $10^\circ\text{--}90^\circ$  with a step size of  $0.01^\circ$ . Scanning electron microscopy (SEM) measurements were carried out

on a field-emission scanning electron microscopy (FE-SEM, FEI Inspect F50). Transmission electron microscopy (TEM) and high-resolution TEM (HRTEM) studies were performed on a FEI TECNAI G2 F20 microscope under an acceleration voltage of 200 kV. The light absorption ability of the prepared sample was investigated by ultraviolet–visible (UV–Vis) diffuse-reflectance spectra (DRS) on a Jindao UV 2600 spectrometer in the wavelength range of 300–800 nm equipped with an integrating sphere, and  $\text{BaSO}_4$  was used as a reflectance standard. The room temperature photoluminescence (PL) properties were measured in ambient conditions. PL measurement was taken on a Hitachi F-4600 spectrophotometer using Xe lamp as excitation source.

### 2.3 Photocatalytic measurements

The photocatalytic performance of the as-prepared sample was evaluated by the degradation of 5 mg/L RhB in aqueous solution under visible light irradiation (Xe lamp, 300 W; visible cut-off filter  $\geq 400 \text{ nm}$ ). In experiment, 30 mg of the BFO photocatalyst was suspended in an aqueous solution (80 mL) of RhB in a reactor chamber. Before visible light irradiation, the suspensions were magnetically stirred in the dark for 1 h to ensure the adsorption–desorption equilibrium between photocatalyst and RhB. After the dark reaction, the solution was irradiated using visible light. At appropriate time intervals, 5 mL of suspension was collected and centrifuged at 9000 rpm for 10 min to separate the catalyst powder from the solution. The concentration of RhB solution was then determined by measuring the maximum absorbance at 554.0 nm using a UV–Vis spectrometer (UV 2600 spectrometer). The degradation percentage was calculated using the following equation:  $(C_0 - C)/C_0 \times 100\%$ , where  $C_0$  and  $C$  denote the absorbance of the characteristic peak of RhB at 554.0 nm before and after illumination. To prevent any self-degradation of RhB, the RhB solution was also photolyzed in the absence of photocatalyst in the same condition.

## 3 Results and discussion

### 3.1 Crystal structure

To identify the structure and the phase purity of the prepared sample, we had performed powder X-ray diffraction (PXRD) studies. Figure 1 shows the X-ray diffraction pattern of BFO powder synthesized under hydrothermal temperature for 48 h. All the diffraction peaks can be indexed with respect to  $R3c$  space group of  $\text{BiFeO}_3$  (JCPDS No. 20-0169), and the crystal structure of the BFO sample is rhombohedral structure, in good agreement with the literature data [20]. In

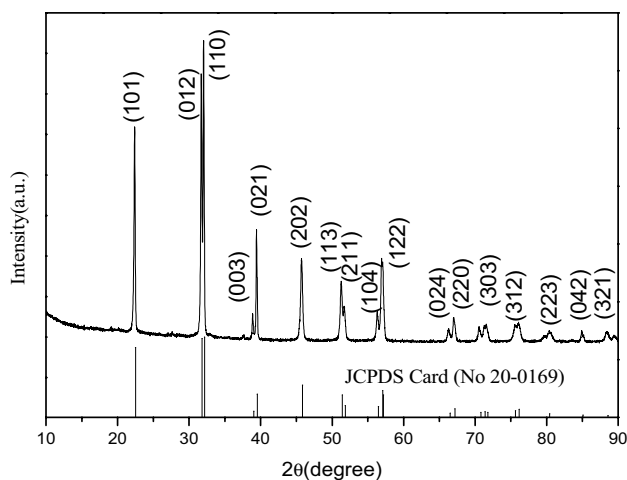


**Fig. 1** XRD pattern of the as-synthesized BFO powder by hydrothermal process

addition, no impurity peaks are observed in the XRD pattern, confirming the high purity of the BFO products.

### 3.2 Morphological analysis

It is well known that PVP, as an important surfactant, is usually used to control the morphologies of nanomaterials [29–31]. Figure 2 shows the morphology of the as-synthesized BFO sample using the 0.5 g of PVP surfactant. Figure 2a shows the FESEM image of BFO nanorods at low magnification and Fig. 2b is the FESEM image of BFO nanorods at high magnification. Figure 2 shows the existence of a large number of BFO nanorods of different sizes, and the length of the observed BFO nanorods is approximately hundreds of

nanometre or several microns, the BFO nanorods have the diameters of 45–350 nm.

To further observe the morphology and the crystal characteristics of the BFO sample, TEM image of the BFO nanorods was displayed in Fig. 3. Figure 3b shows the magnified TEM image of an individual BFO nanorod. Figure 3c is a HRTEM image of a typical portion of a corresponding BFO nanorod, displaying an intact, orderly, single-crystalline structure. The selected area electron diffraction (SAED) pattern is presented in Fig. 3d. The planes with interplanar spacing of 0.258, 0.482 and 0.278 nm are corresponding to the (111) (100) and (110) crystal faces, respectively.

### 3.3 UV–Vis DRS analysis

The optical property of BFO sample was investigated by UV–Vis diffuse reflectance spectroscopy, as shown in Fig. 4. The absorption spectrum shows that the absorption band edge of BFO nanorods appeared at 565 nm, which was similar to those previously reported [4, 32], indicating that BFO sample absorbs an amount of visible light. This absorption can be attributed to the electronic band gap transition from the valence band (O 2p orbital) to the conduction band (Fe 3d orbital) ( $O_{2p}^{2-} \rightarrow Fe_{3d}^{3+}$ ) [33, 34]. The band gap energy ( $E_g$ ) of BFO could be calculated from the plot of the Kubelka–Munk function [35]  $[(Ah\nu)^2$  as photon energy ( $h\nu$ )] for the direct band gap semiconductor, as shown in the inset of Fig. 4. This relationship gives the  $E_g$  by extrapolating the straight portion of  $(Ah\nu)^2$  against  $h\nu$  plot to the point  $(Ah\nu)=0$ . The band gap is estimated about 2.16 eV by the linear extrapolation, which is quite comparable with previous results 2.16 eV [36] and 2.18 eV [8] and smaller than that of the bulk BFO (2.8 eV) [37]. Therefore, such narrow

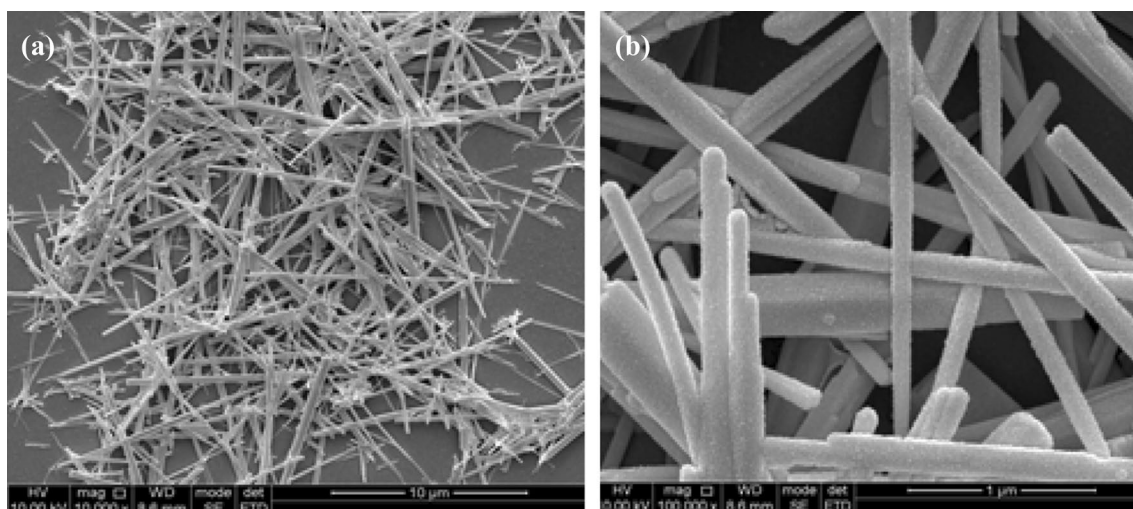


**Fig. 2** **a** FESEM image of BFO nanorods at low magnification. **b** FESEM image of BFO nanorods at high magnification

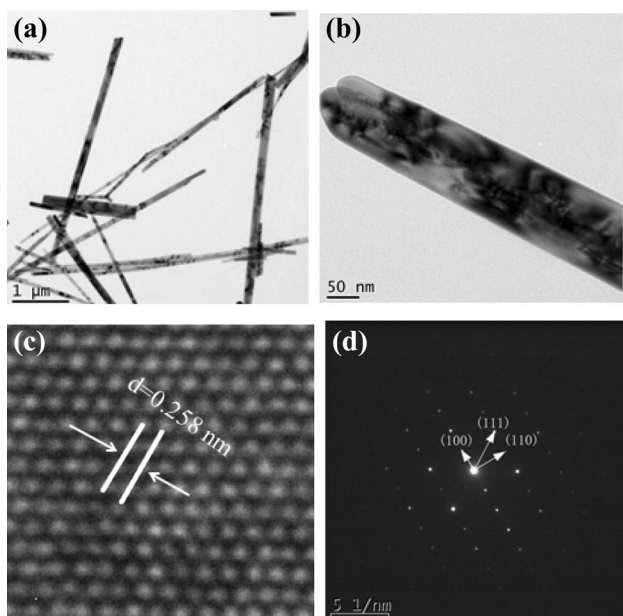


**Fig. 3** TEM image of BFO nanorods (a), individual BFO nanorod (b), HRTEM image of a typical portion of a corresponding BFO nanorod showing the crystalline structure (c), SAED pattern of an individual BFO nanorod (d)

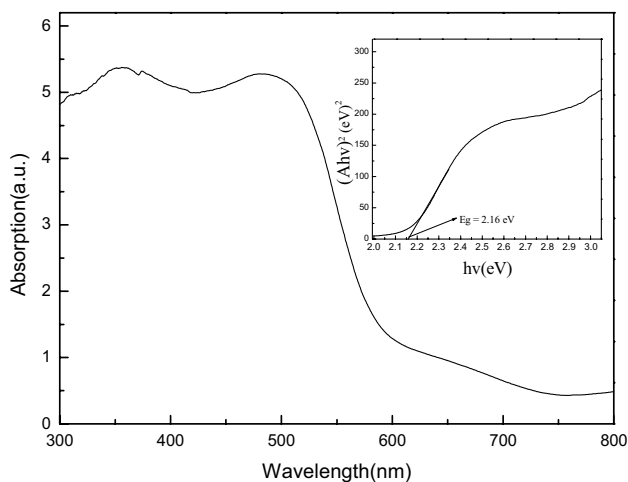


**Fig. 4** UV-Vis DRS spectrum of the BFO nanorods, the inset shows the band gap estimated for BFO

band gap is beneficial for implying possible application in potential sunlight driven photocatalyst.

### 3.4 PL spectrum analysis

As known, the PL properties of semiconductor can reflect the capture and transfer behaviour of charge carriers in semiconductors [38, 39]. The PL emission intensity can reflect the recombination of photoexcited electrons and holes, and

the stronger PL emission intensity represents higher recombination rate of photoexcited electrons and holes [39]. Figure 5 shows the PL spectrum of BFO nanorods at the excitation wavelength of 400 nm. The main peak of PL emission at 602 nm is corresponding to the radiative emission due to the recombination of electron-hole pairs. However in PL spectrum a kink is appearing before main peak at 602 nm, which is similar to what has been reported by Liu [40]. As for the origin of this kink, there was scant literature available. In principle, any other emissions, except for the intrinsic emission from the band-to-band transition, should originate from the defects/impurity levels inside the bandgap [41].

### 3.5 Photocatalytic performance

The photocatalytic activity of BFO sample was evaluated by the photodegradation of RhB aqueous solution under visible light ( $\lambda \geq 400$  nm) irradiation after adsorption/desorption equilibration. Figure 6a shows the photocatalytic degradation of RhB by BFO photocatalyst under visible light. The blank experimental result is also shown in Fig. 6a, which indicates that the RhB concentration was nearly unchanged during the whole irradiation time without the photocatalyst, suggesting that RhB is a stable pollution. When BFO photocatalyst particles were added into the RhB aqueous solution, RhB was gradually degraded during the visible light irradiation process. After 270 min irradiation time, the decomposition rate was 25.4%, which was slightly higher than that of the previous results (22.3%) with 0.3 g of the BFO nanoparticle photocatalyst suspended in an aqueous solution (100 mL) of RhB [4], and the catalytic performance is not too considerable, which may be attributed to the surface defects of one-dimensional BFO nanorods with high surface-to-volume ratio. The surface state plays a very

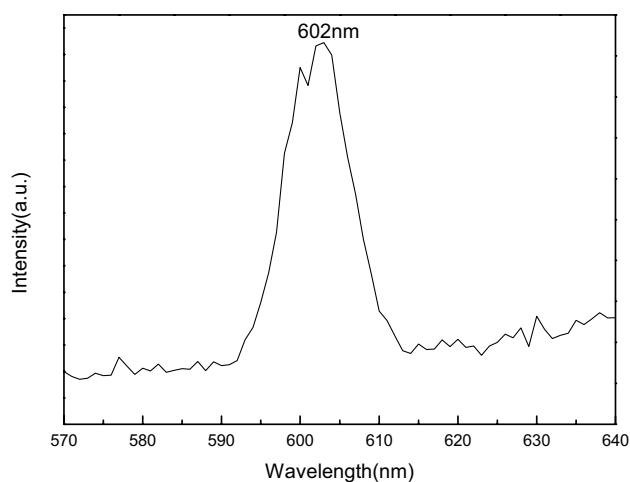


**Fig. 5** The PL spectrum of BFO nanorods

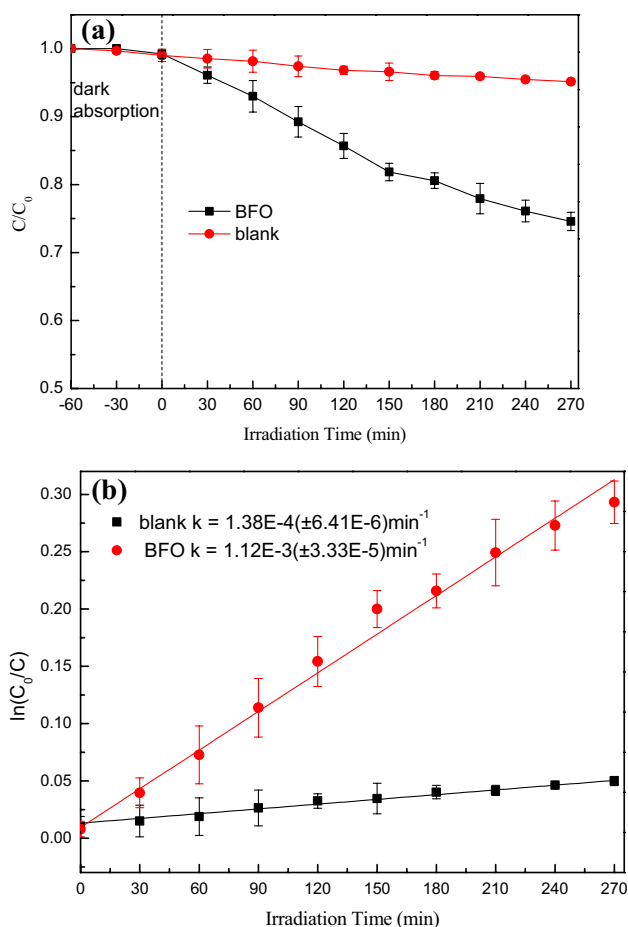


**Fig. 6** **a** Photocatalytic degradation of RhB as a function of the irradiation time under visible light for the as-prepared BFO sample; **b** plot of  $\ln(C_0/C)$  as a function of visible irradiation time for photocatalysis of RhB solution

important role in determining carrier transport and optical excitation/recombination properties [42].

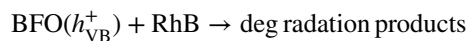
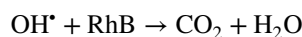
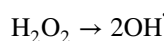
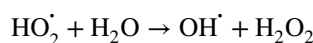
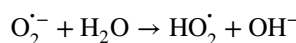
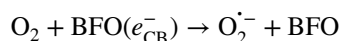
The reaction kinetics of RhB degradation for BFO nanorods photocatalyst was analyzed by fitting the experimental data in Fig. 6a according to the Langmuir–Hinshelwood model, as expressed by the following equation [43]:

$$\ln \frac{C_0}{C} = kt \quad (1)$$

where  $C_0$  and  $C$  are the concentrations of RhB at  $t_0$  and  $t$ , respectively, and  $k$  is the pseudo-first-order rate constant of photodegradation ( $\text{min}^{-1}$ ). The linear fitting curves of  $\ln(C_0/C)$  versus irradiation time ( $t$ ) are shown in Fig. 6b. From the linear fitting curves, the RhB degradation rate constant  $k$  was calculated to be  $1.38 \times 10^{-4}$ ,  $1.12 \times 10^{-3} \text{ min}^{-1}$  for the blank sample and BFO, respectively.

Based on the above experimental results, a possible mechanism of RhB degradation by BFO sample

is as follows. Under the illumination of visible light ( $\lambda \geq 400 \text{ nm}$ ), with photon energy exceeding the band gap of the BFO, the photogenerated electrons and holes are generated, which could be either trapped at defect sites or diffused toward the surface of the photocatalyst. The photoinduced electrons transferred from the bulk BFO to the surface of the photocatalyst could capture the adsorbed  $\text{O}_2$  and reduce it to superoxide radical anion ( $\text{O}_2^{\cdot-}$ ) and hydroxyl radicals ( $\text{OH}^{\cdot}$ ), which then participate in photocatalytic degradation of RhB. Finally, the organic pollutants may be decomposed into  $\text{CO}_2$ ,  $\text{H}_2\text{O}$ , or inorganic ions. The proposed photodegradation mechanism of BFO for RhB could be described as follows: [44]



where  $e_{\text{CB}}^-$  and  $h_{\text{VB}}^+$  stand for the electron in the conduction band and hole in the valence band, respectively.

## 4 Conclusions

In this work, one-dimensional, single-crystalline BFO nanorods with rhombohedral crystal structure were successfully prepared by polyvinylpyrrolidone (PVP)-assisted hydrothermal process. FESEM and TEM images indicate that the as-prepared  $\text{BiFeO}_3$  nanoparticles are the shape of nanorods with different sizes. The energy band gap is found to be about 2.16 eV, which are suitable for photocatalytic degradation of RhB dye under visible-light irradiation. The photocatalytic result revealed that the as-prepared BFO nanorods exhibit photocatalytic activity under visible light irradiation ( $\lambda \geq 400 \text{ nm}$ ), and 25.4% RhB was decomposed after 270 min irradiation time. Meanwhile, a possible photocatalytic mechanism of BFO nanorods was critically discussed.

**Acknowledgements** This work was supported by the National Natural Science Foundation of China (Grant No. 11847315), Educational Commission of Zhejiang Province of China (Grant No. Y201737491) and Huzhou University Scientific Research Project (Grant No. 2017XJXM45).

## References

1. J. Wang, J.B. Neaton, H. Zheng, V. Nagarajan, S.B. Ogale, B. Liu, D. Viehland, V. Vaithyanathan, D.G. Schlom, U.V. Waghmare, N.A. Spaldin, K.M. Rabe, M. Wuttig, R. Ramesh, *Science* **299**, 1719–1722 (2003)
2. G. Catalan, J.F. Scott, *Adv. Mater.* **21**, 2463–2485 (2009)
3. S. Fusil, V. Garcia, A. Barthélémy, M. Bibes, *Annu. Rev. Mater. Res.* **44**, 91–116 (2014)
4. N. Zhang, D. Chen, F. Niu, S. Wang, L.S. Qin, Y.X. Huang, *Sci. Rep.* **6**, 26467 (2016)
5. S. Li, Y.H. Lin, B.P. Zhang, Y. Wang, C.W. Nan, *J. Phys. Chem. C* **114**, 2903–2908 (2010)
6. H. Maleki, *J. Mater. Sci.* **29**, 11860–11869 (2018)
7. H.C. Wang, Y.H. Lin, Y.N. Feng, Y. Shen, *J. Electroceram.* **31**, 271–274 (2013)
8. F. Gao, X.Y. Chen, K.B. Yin, S. Dong, Z.F. Ren, F. Yuan, T. Yu, Z.G. Zou, J.M. Liu, *Adv. Mater.* **19**, 2889–2892 (2007)
9. W. Wang, N. Li, Y. Chi, Y. Li, W. Yan, X. Li, C. Shao, *Ceram. Int.* **39**, 3511–3518 (2013)
10. W. Ji, K. Yao, Y.F. Lim, Y.C. Liang, A. Suwardi, *Appl. Phys. Lett.* **103**, 062901 (2013)
11. Y.N. Huo, Y. Jin, Y. Zhang, *J. Mol. Catal. A* **331**, 15–20 (2010)
12. Y.P. Lv, J. Xing, C.C. Zhao, D.M. Chen, J.J. Dong, H.Y. Hao, X.W. Wu, Z.Y. Zheng, *J. Mater. Sci.* **26**, 1525–1532 (2015)
13. F. Niu, T. Gao, N. Zhang, Z. Chen, Q.L. Huang, L.S. Qin, X.G. Sun, Y.X. Huang, *J. Nanosci. Nanotechnol.* **15**, 9693–9698 (2015)
14. S. Moharana, M.K. Mishra, M. Chopkar, R.N. Mahaling, *Polym. Bull.* **74**, 3707–3719 (2017)
15. G.Y. He, J.H. Zhang, Y. Hu, Z.G. Bai, C.H. Wei, *Appl. Catal. B* **250**, 301–312 (2019)
16. D. Wang, A. Pierre, M.G. Kibria, K. Cui, X. Han, K.H. Bevan, H. Guo, S. Paradis, A.R. Hakima, Z. Mi, *Nano. Lett.* **11**, 2353–2357 (2011)
17. X.H. Zhang, H.Y. Liu, B. Zheng, Y.H. Lin, D.P. Liu, C.W. Nan, *J. Nanomater.* **2013**, 1–7 (2013)
18. S. Li, J.M. Zhang, M.G. Kibria, Z. Mi, M. Chaker, D.L. Ma, R. Nechache, F. Rosei, *Chem. Commun.* **49**, 5856–5858 (2013)
19. I. Hochbaum, P. Yang, *Chem. Rev.* **110**, 527–546 (2010)
20. B. Liu, ZDu Hu, *Chem. Comm.* **47**, 8166–8168 (2011)
21. S. Li, R. Nechache, C. Harnagea, L. Nikolova, F. Rosei, *Appl. Phys. Lett.* **101**, 192903 (2012)
22. L. Wu, W.B. Sui, C.H. Dong, C. Zhang, C.J. Jiang, *Appl. Surf. Sci.* **384**, 368–375 (2016)
23. X.Y. Zhang, C.W. Lai, X. Zhao, D.Y. Wang, J.Y. Da, *Appl. Phys. Lett.* **87**, 143102 (2005)
24. X. Xu, T. Qian, G. Zhang, T. Zhang, G. Li, W. Wang, X. Li, *Chem. Lett.* **36**, 112–113 (2007)
25. S.H. Xie, J.Y. Li, R. Proksch, Y.M. Liu, Y.C. Zhou, Y.Y. Liu, Y. Ou, L.N. Lan, Y. Qiao, *Appl. Phys. Lett.* **93**, 222904 (2008)
26. K. Prashanthi, R. Gaikwad, T. Thundat, *Nanotechnol.* **24**, 505710 (2013)
27. C.L. Fu, F. Sun, J.X. Hao, R.L. Gao, W. Cai, G. Chen, X.L. Deng, *J Mater Sci* **27**, 8242–8246 (2016)
28. T.T. Carvalho, P.B. Tavares, *Mater. Lett.* **62**, 3984–3986 (2008)
29. X. Wang, W. Mao, Q. Zhang, Q. Wang, Y. Zhu, J. Zhang, T. Yang, J. Yang, X.A. Li, W. Huang, *J. Alloys Compd.* **677**, 288–293 (2016)
30. F. Qin, H.P. Zhao, G.F. Li, H. Yang, J. Li, R.M. Wang, Y.L. Liu, J.C. Hu, H.Z. Sun, R. Chen, *Nanoscale* **6**, 5402–5409 (2014)
31. X.F. Wang, W.W. Mao, Q.X. Zhang, Q. Wang, Y.Y. Zhu, J. Zhang, T. Yang, J.P. Yang, X. Li, W. Huang, *J. Alloys Compd.* **667**, 288–293 (2016)
32. J.Y. Wang, Y.W. Wei, J.J. Zhang, L.D. Ji, Y.X. Huang, Z. Chen, *Mater. Lett.* **124**, 242–244 (2014)
33. R. Dhanalakshmi, M. Muneeswaran, P.R. Vanga, M. Ashok, N.V. Giridharan, *Appl. Phys. A* **122**, 1–14 (2016)
34. S. Falahatnezhad, H. Maleki, *J. Mater. Sci.* **29**, 17360 (2018)
35. C. Clementi, C. Miliani, G. Verri, S. Sotiropoulou, A. Romani, B.G. Brunetti, A. Sqamellotti, *Appl. Spectrosc.* **63**, 1323–1329 (2009)
36. F. Niu, D. Chen, L.S. Qin, T. Gao, N. Zhang, S. Wang, Z. Chen, J.Y. Wang, X.G. Sun, Y.X. Huang, *Sol. Energy Mater. Sol. Cells* **143**, 386–396 (2015)
37. X.S. Xu, T.V. Brinzari, S. Lee, Y.H. Chu, L.W. Martin, A. Kumar, S. McGill, R.C. Rai, R. Ramesh, V. Gopalan, S.W. Cheong, J.L. Musfeldt, *Phys. Rev. B* **79**, 134425 (2009)
38. M.D.L.R. Peralta, U. Pal, R.S. Zeferino, A.C.S. Appl. Mater. Interfaces **4**, 4807–4816 (2012)
39. Y. Zhang, Z.Y. Cai, X.M. Ma, *Phys B* **479**, 101–106 (2015)
40. Y. Liu, R.Z. Zuo, S.S. Qi, *J Mol Catal A: Chem* **376**, 1–6 (2013)
41. X.M. Chen, H. Zhang, T. Wang, F.F. Wang, W.Z. Shi, *Phys. Status Solidi A* **209**, 1456–1460 (2012)
42. L.S. Mende, J.L. MacManus-Driscoll, *Mater. Today* **10**, 40–48 (2007)
43. L. Ge, C.C. Han, J. Liu, Y.F. Li, *Appl. Catal. A* **409–410**, 215–222 (2011)
44. S. Khanchandani, S. Kundu, A. Patra, A.K. Ganguli, *J. Phys. Chem. C* **116**, 23653–23662 (2012)

**Publisher's Note** Springer Nature remains neutral with regard to jurisdictional claims in published maps and institutional affiliations.